



CHALMERS
UNIVERSITY OF TECHNOLOGY

Extremely anisotropic van der Waals thermal conductors

Downloaded from: <https://research.chalmers.se>, 2024-04-23 07:16 UTC

Citation for the original published paper (version of record):

Kim, S., Mujid, F., Rai, A. et al (2021). Extremely anisotropic van der Waals thermal conductors. Nature, 597(7878): 660-665. <http://dx.doi.org/10.1038/s41586-021-03867-8>

N.B. When citing this work, cite the original published paper.

Extremely anisotropic van der Waals thermal conductors

<https://doi.org/10.1038/s41586-021-03867-8>

Received: 5 February 2021

Accepted: 29 July 2021

Published online: 29 September 2021

Open access

 Check for updates

Shi En Kim¹, Fauzia Mujid², Akash Rai³, Fredrik Eriksson⁴, Joonki Suh^{2,5}, Preeti Poddar², Ariana Ray⁶, Chibeom Park^{1,5}, Erik Fransson⁴, Yu Zhong², David A. Muller⁶, Paul Erhart^{4,✉}, David G. Cahill^{3,✉} & Jiwoong Park^{1,2,5,✉}

The densification of integrated circuits requires thermal management strategies and high thermal conductivity materials^{1–3}. Recent innovations include the development of materials with thermal conduction anisotropy, which can remove hotspots along the fast-axis direction and provide thermal insulation along the slow axis^{4,5}. However, most artificially engineered thermal conductors have anisotropy ratios much smaller than those seen in naturally anisotropic materials. Here we report extremely anisotropic thermal conductors based on large-area van der Waals thin films with random interlayer rotations, which produce a room-temperature thermal anisotropy ratio close to 900 in MoS₂, one of the highest ever reported. This is enabled by the interlayer rotations that impede the through-plane thermal transport, while the long-range intralayer crystallinity maintains high in-plane thermal conductivity. We measure ultralow thermal conductivities in the through-plane direction for MoS₂ ($57 \pm 3 \text{ mW m}^{-1} \text{ K}^{-1}$) and WS₂ ($41 \pm 3 \text{ mW m}^{-1} \text{ K}^{-1}$) films, and we quantitatively explain these values using molecular dynamics simulations that reveal one-dimensional glass-like thermal transport. Conversely, the in-plane thermal conductivity in these MoS₂ films is close to the single-crystal value. Covering nanofabricated gold electrodes with our anisotropic films prevents overheating of the electrodes and blocks heat from reaching the device surface. Our work establishes interlayer rotation in crystalline layered materials as a new degree of freedom for engineering-directed heat transport in solid-state systems.

Anisotropic thermal conductors, in which heat flows faster in one direction than in another, can be characterized by the thermal conductivity anisotropy ratio $\rho (= \kappa_{\parallel}/\kappa_{\perp})$ between the thermal conductivities along the fast axis (κ_{\parallel}) and the slow axis (κ_{\perp}). One common way to engineer ρ in fully dense solids is via nanostructuring⁶, such as fabricating inorganic superlattices^{7–11} or designing symmetry-breaking crystal architectures in a single material¹². However, such engineered materials have relatively small ρ values of less than 20 at room temperature. Conversely, some natural crystalline materials have an intrinsically large ρ (for example, graphite¹ and hexagonal boron nitride (hBN)¹³, with $\rho \approx 340$ and 90 respectively), but they are often difficult to process scalably for thin film integration. Some of these films may also lack the electrical or optical properties necessary for functional device applications.

To design materials with higher ρ that are also suitable for real-world applications, an approach needs to be developed to include three key features: (1) a candidate material with intrinsically high κ_{\parallel} , usually one with efficient phonon-mediated thermal transport; (2) a method to substantially reduce κ_{\perp} without affecting κ_{\parallel} ; and (3) facile, scalable production and integration of such a material with precise control of the material dimensions (for example, film thickness). Layered van der Waals (vdW) materials such as graphite and transition metal dichalcogenides

(TMDs) provide an ideal material platform for designing such high- ρ materials. They generally have excellent intrinsic in-plane thermal conductivities (κ_{\parallel}) in single-crystalline form. Previous studies have also measured record-low thermal conductivities in nanocrystalline vdW films (for example, WSe₂)^{14–17} and heterostructures¹⁸. One currently missing capability, however, is an approach for significantly decreasing the out-of-plane thermal conductivity (κ_{\perp}) while maintaining high κ_{\parallel} .

TMD films with interlayer rotations

Here we show that such capability is provided by interlayer rotations, as illustrated in Fig. 1a. Interlayer rotation breaks the through-plane translational symmetry at the atomic scale while retaining in-plane long-range crystallinity in each monolayer, thereby providing an effective means for suppressing only κ_{\perp} . For this, we produce large-area TMD films without interlayer registry (referred to here as r-TMD), which possess long-range crystallinity in-plane and relative lattice rotations at every interlayer interface (Fig. 1b). The films are produced in large-scale using two steps: wafer-scale growth of continuous TMD monolayers (polycrystalline; domain size D) and layer-by-layer stacking in vacuum using previously reported methods^{19,20} (see Methods).

¹Pritzker School of Molecular Engineering, University of Chicago, Chicago, IL, USA. ²Department of Chemistry, University of Chicago, Chicago, IL, USA. ³Department of Materials Science and Engineering and Materials Research Laboratory, University of Illinois at Urbana-Champaign, Urbana, IL, USA. ⁴Department of Physics, Chalmers University of Technology, Gothenburg, Sweden. ⁵James Franck Institute, University of Chicago, Chicago, IL, USA. ⁶School of Applied and Engineering Physics, Cornell University, Ithaca, NY, USA. ✉e-mail: erhart@chalmers.se; d-cahill@illinois.edu; jwpark@uchicago.edu

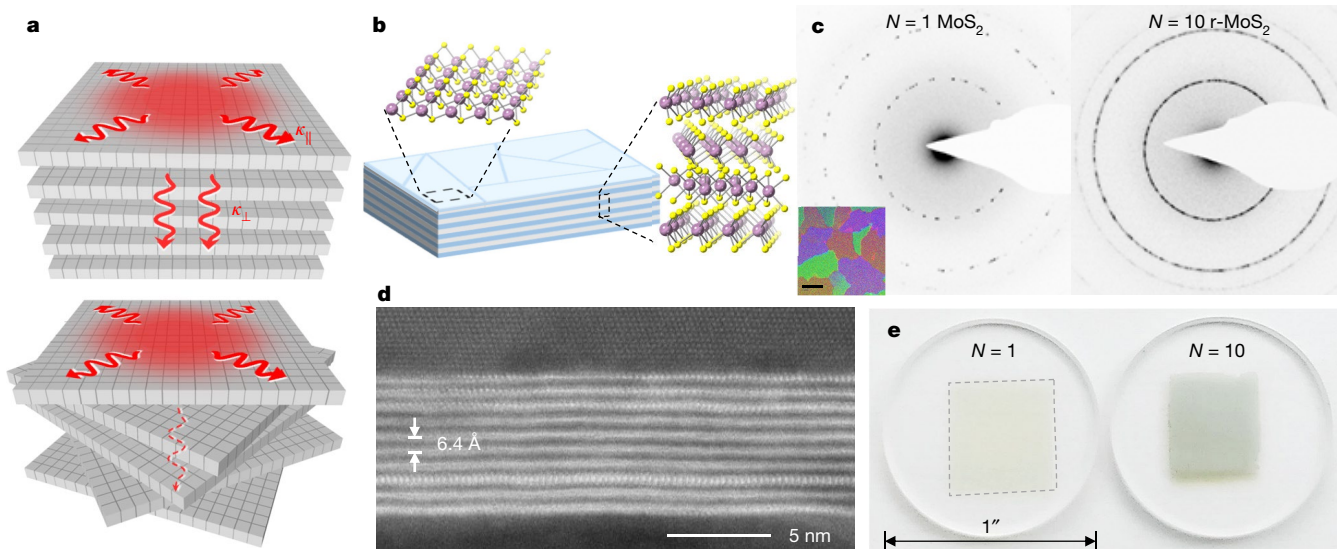


Fig. 1 | Structure of r-TMD films. **a**, Conceptual strategy for engineering thermal anisotropy in a single material system, using random interlayer rotation in polycrystalline vdW layered materials. **b**, Schematic of an r-MoS₂ film with random crystalline orientation. **c**, Greyscale-inverted TEM electron diffraction patterns probed from a 500 nm × 500 nm area of a monolayer and

an $N = 10$ r-MoS₂ film. Inset: darkfield TEM image of a monolayer; the scale bar denotes 400 nm and the colours denote different domain orientations from different crystal domains. **d**, HAADF-STEM image of a cross-section of an $N = 10$ r-MoS₂ film on AlO_x coated with Al, with an interlayer spacing of 6.4 Å. **e**, Large-area MoS₂ films transferred onto 1-inch diameter fused silica substrates.

The transmission electron microscopy (TEM) diffraction (Fig. 1c, left) and darkfield (inset) images from a representative MoS₂ monolayer show that it comprises large ($D \approx 1 \mu\text{m}$), randomly oriented crystalline domains, which connect laterally to form a continuous polycrystalline film. The vacuum stacking generates r-TMD films with a precise layer number (N) and high-quality interfaces²⁰ with interlayer rotation at every stacked interface. The TEM diffraction pattern of $N = 10$ r-MoS₂ (Fig. 1c, right) shows a ring-like pattern due to the significant increase in the number of diffraction spots, emphasizing the random crystalline orientation in the through-plane direction. Clean and well-defined interfaces can be seen from the cross-sectional high-angle annular darkfield scanning TEM (HAADF-STEM) images of r-MoS₂ (Fig. 1d and Extended Data Fig. 1; see Methods). The monolayers have a uniform interlayer spacing $d \approx 6.4 \text{ Å}$ (see Methods and Extended Data Fig. 2), which is close to the expected value (6.5 Å) for twisted MoS₂ multilayers²¹. Both the growth and stacking steps are scalable, as shown by the optical images of $N = 1$ and $N = 10$ r-MoS₂ films ($\sim 1 \text{ cm}^2$) in Fig. 1e and as demonstrated later in Fig. 4. The large-scale uniformity of these films also enables precise and reproducible measurements with minimal spatial variation (Extended Data Fig. 3a–c). In our experiments, r-MoS₂ or r-WS₂ films with different N (up to 22) are transferred onto a sapphire wafer for the measurements of κ_{\perp} or suspended over a holey TEM grid (Fig. 3a) for the measurements of κ_{\parallel} .

Ultralow out-of-plane conductivity

In Fig. 2, we illustrate κ_{\perp} of r-TMD films, which is measured using time domain thermoreflectance (TDTR; Fig. 2a, inset; see Methods). A stream of laser pulses (pump) heats up the surface of an Al pad deposited on an r-TMD film on sapphire and produces a temperature-sensitive thermoreflectance signal ($-V_{\text{in}}/V_{\text{out}}$ in Fig. 2a), which is measured with a probe pulse after a varying time delay (for cooling). Figure 2a shows three representative curves measured from r-MoS₂ with $N = 1, 2$ and 10. The curves flatten with increasing N , suggesting that heat dissipation slows down significantly. Fitting these curves using a heat diffusion model (solid lines, Fig. 2a) enables us to obtain R_{TDR} , the total thermal resistance between the Al transducer layer and sapphire across the r-TMD film for different N .

Figure 2b shows R_{TDR} versus N for r-MoS₂ ($N \leq 22$; solid circles) and r-WS₂ ($N \leq 10$; open circles) measured under ambient conditions. We make two observations. First, R_{TDR} monotonically increases with N . Second, R_{TDR} varies linearly with N for $N \geq 2$. These observations confirm that the through-plane thermal transport in r-TMD films is diffusive in nature, in contrast to the ballistic transport reported in few-layer single-crystalline MoS₂ (as thick as 240 nm)^{22,23}. A single parameter κ_{\perp} characterizes the thermal resistance across r-MoS₂ (or r-WS₂) using the equation $R_{\text{TDR}} = R_0 + Nd/\kappa_{\perp}$, where Nd is the total film thickness, and R_0 is a constant corresponding to the total interface resistance (r-TMD/Al and r-TMD/sapphire; see Extended Data Table 1). Therefore, we apply linear fitting to the data ($N \geq 2$) in Fig. 2b (solid lines) to determine κ_{\perp} of r-MoS₂ alone, regardless of the quality and chemical nature of the top and bottom interfaces (see Methods and Extended Data Fig. 3d), which can potentially be altered by metal deposition^{24,25}. We measure $\kappa_{\perp} = 57 \pm 3 \text{ mW m}^{-1} \text{ K}^{-1}$ for r-MoS₂ and $\kappa_{\perp} = 41 \pm 3 \text{ mW m}^{-1} \text{ K}^{-1}$ for r-WS₂, which are similar to the lowest value ever observed in a fully dense solid¹⁵ and comparable to the thermal conductivity of ambient air ($\sim 26 \text{ mW m}^{-1} \text{ K}^{-1}$). These values are approximately two orders of magnitude smaller than those of single-crystalline MoS₂ ($2\text{--}5 \text{ W m}^{-1} \text{ K}^{-1}$)^{26,27} or WS₂ ($\sim 3 \text{ W m}^{-1} \text{ K}^{-1}$)²⁷, despite the r-TMD films having the same chemical composition as their bulk counterparts as well as clean interfaces (Fig. 1d). This strongly suggests that the main difference, the interlayer rotation, is the principal cause for the ultralow κ_{\perp} in these r-TMD films. Furthermore, repeating similar TDTR experiments on r-MoS₂ at different temperatures (T) produces a relatively flat $\kappa_{\perp}(T)$ curve (green stars, Fig. 2c), a behaviour different from the decreasing κ_{\perp} with T seen in bulk MoS₂ (blue squares, lower Fig. 2c).

To understand the microscopic mechanisms that give rise to the dramatic reduction in κ_{\perp} , we carry out homogeneous non-equilibrium molecular dynamics (HNEMD) simulations for the model structures of r-MoS₂ and bulk MoS₂ (see Methods and Extended Data Table 2)^{28–30}. Figure 2c shows κ_{\parallel} and κ_{\perp} of r-MoS₂ (solid circles) and bulk MoS₂ (empty circles) calculated from our molecular dynamics (MD) simulations at different temperatures. The calculated κ_{\perp} drops by a factor of more than 20, from $3.7 \pm 0.5 \text{ W m}^{-1} \text{ K}^{-1}$ in bulk MoS₂ to $0.16 \pm 0.04 \text{ W m}^{-1} \text{ K}^{-1}$ in r-MoS₂ at 300 K, and also does not decrease with T , suggesting a transition away from the phonon-limited thermal transport mechanism observed in bulk MoS₂.

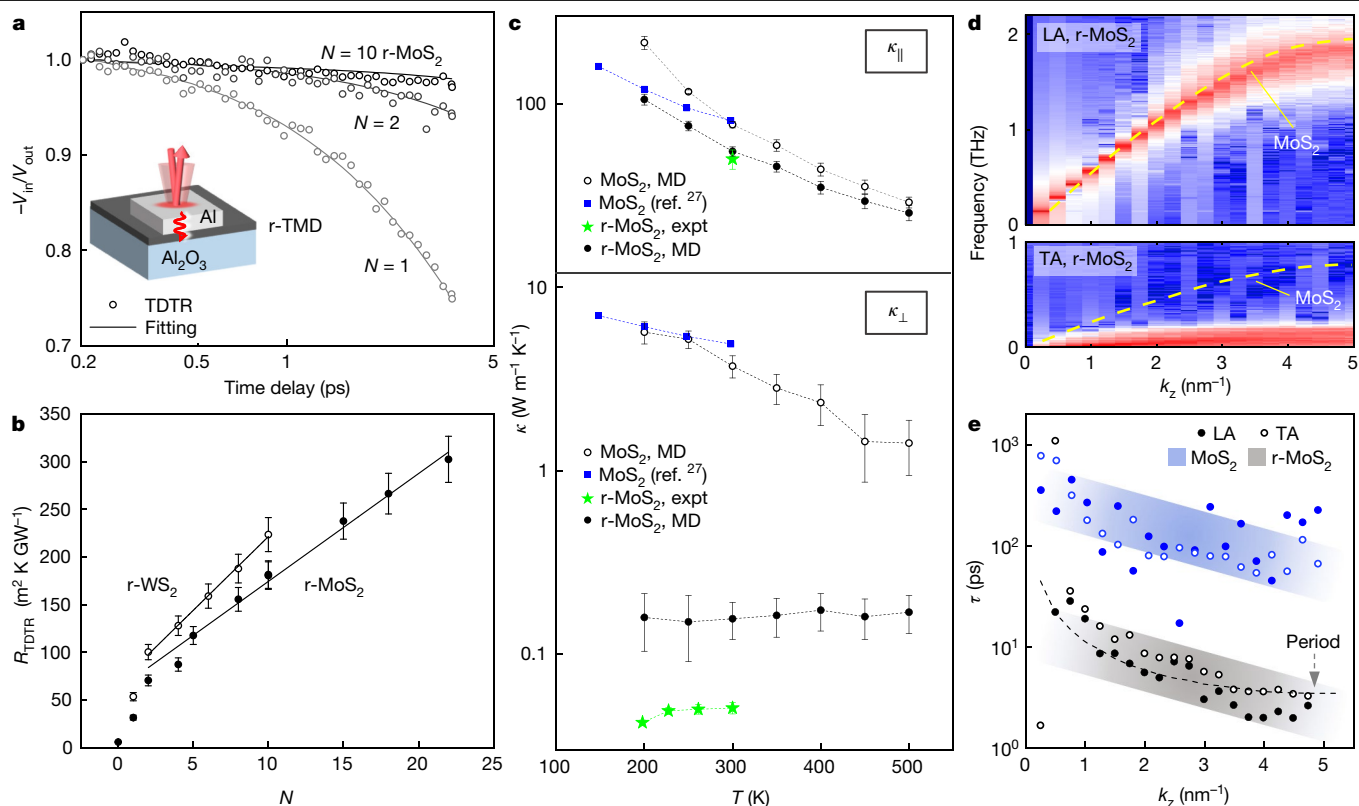


Fig. 2 | Through-plane thermal properties of r-MoS₂. **a**, TDTR heat dissipation curves of *N*-layer r-MoS₂ films. Inset: TDTR sample geometry. **b**, Measured thermal resistances across r-TMD films, where the error bars are the TDTR measurement uncertainties. The thermal conductivities for r-MoS₂ and r-WSe₂ are calculated from the slope using the formula $R_{\text{TDR}} = R_0 + Nd/\kappa_{\perp}$, whereby R_0 is the total interfacial thermal resistance. **c**, Experiment and MD simulation results of $\kappa(T)$ of MoS₂ and r-MoS₂ films. The error bars to the MD

simulations originate from the simulation uncertainties. The dotted lines connecting the individual data points are guides to the eye. **d**, LA (top) and TA (bottom) phonon dispersion curves of r-MoS₂ along the Γ -A direction. The dotted lines denote the acoustic curves corresponding to bulk MoS₂. **e**, Lifetime of LA and TA phonons parallel to the Γ -A direction in bulk and r-MoS₂. The dashed line is the LA mode vibration period derived from the dispersion curve in **d**.

Further analysis of the vibrational spectrum of r-MoS₂ enables us to break down the reduction in κ_{\perp} in terms of the changes in the group velocities (v_g) and lifetimes (τ), which are the two factors that determine the thermal conductivity according to Boltzmann transport theory. Figure 2d shows that the v_g of the through-plane longitudinal acoustic (LA) mode in r-MoS₂ remains similar to that of bulk MoS₂ (dashed lines), but the transverse acoustic (TA) modes in r-MoS₂ undergo extreme softening with their v_g s practically vanishing³¹. This implies a loss of resistance with respect to lateral shear, consistent with the low-frequency Raman spectra of r-MoS₂ films (see Methods and Extended Data Fig. 4) and previous calculations^{32,33}. In addition, the τ of both the LA and the TA modes (Fig. 2e) in r-MoS₂ are more than one order of magnitude smaller than in bulk MoS₂, with the LA lifetimes being close to the period of the LA mode vibration (dashed line). From these results, the median mean free path $\tilde{l} = v_g\tau$ for the LA modes is estimated to be 2 nm, suggesting that the heat-carrying LA modes are strongly scattered and that a larger D is unlikely to significantly affect κ_{\perp} since $D \gg \tilde{l}$. Overall, the strongly suppressed TA modes, indicating a loss of resistance to lateral shear, and the overdamping of the LA modes as the main heat carriers, lead to extremely inefficient thermal transport along the through-plane direction in r-MoS₂. Along with the nearly temperature-independent κ_{\perp} , this result suggests a glass-like conduction mechanism.

In-plane conductivity and anisotropy

In contrast to κ_{\perp} , κ_{\parallel} remains high in our simulations with only a modest reduction compared to the ideal bulk crystal (less than a factor of

two at 300 K; Fig. 2c). This is indeed what we observe in our Raman thermometry experiments as discussed in Fig. 3 (see Methods). We direct a focused laser spot ($\lambda = 532$ nm) at the centre of a suspended r-MoS₂ film (Fig. 3a; hole diameter of 5 μm , at 15 torr), which increases its temperature (ΔT) locally upon absorbing laser power P_{abs} . ΔT is then measured using the temperature-sensitive Raman peak shift ($\Delta\omega$) using a sensitivity factor ($|d\omega/dT|$) independently measured for each sample. Examples of Raman spectra measured for $N = 2$ are shown in Fig. 3b.

Figure 3c plots $\Delta\omega$ versus P_{abs} for r-MoS₂ with different N (2 to 5). The slope of the linear fit ($|d(\Delta\omega)/dP_{\text{abs}}|$), which is inversely proportional to the in-plane thermal conductance of the film, is plotted in the inset (solid dots; $D \approx 1 \mu\text{m}$). We again observe a linear relation, which indicates that κ_{\parallel} is well defined for r-MoS₂ independent of N , similar to the case of κ_{\perp} . Using a simple diffusion model with radial symmetry (see Methods and Extended Data Fig. 5c for calculation details and other input measurements), we calculate a high κ_{\parallel} value of $50 \pm 6 \text{ W m}^{-1} \text{ K}^{-1}$. This value is similar to the predictions of our MD simulations (Fig. 2c) and consistent with previous reports of Raman thermometry on single-crystalline monolayer MoS₂ (35–84 $\text{W m}^{-1} \text{ K}^{-1}$) at room temperature^{34–37}. The κ_{\parallel} of these r-MoS₂ films is close to the intrinsic phonon-limited value despite the films being made of polycrystalline monolayers. This result is further supported by our additional measurements on continuous r-MoS₂ films with a smaller $D \approx 400$ nm (open dots, dashed lines, Fig. 3c inset; Extended Data Fig. 5e). The measured value of $\kappa_{\parallel} \approx 44 \pm 6 \text{ W m}^{-1} \text{ K}^{-1}$ is within the margin of error of that of the $D \approx 1 \mu\text{m}$ films. This suggests that the phonon mean free path is smaller than 400 nm, which is consistent with previous reports^{23,38–42}. Furthermore, the measured in-plane conductance decreases with T (Extended Data Fig. 6a). This further confirms the phonon-mediated

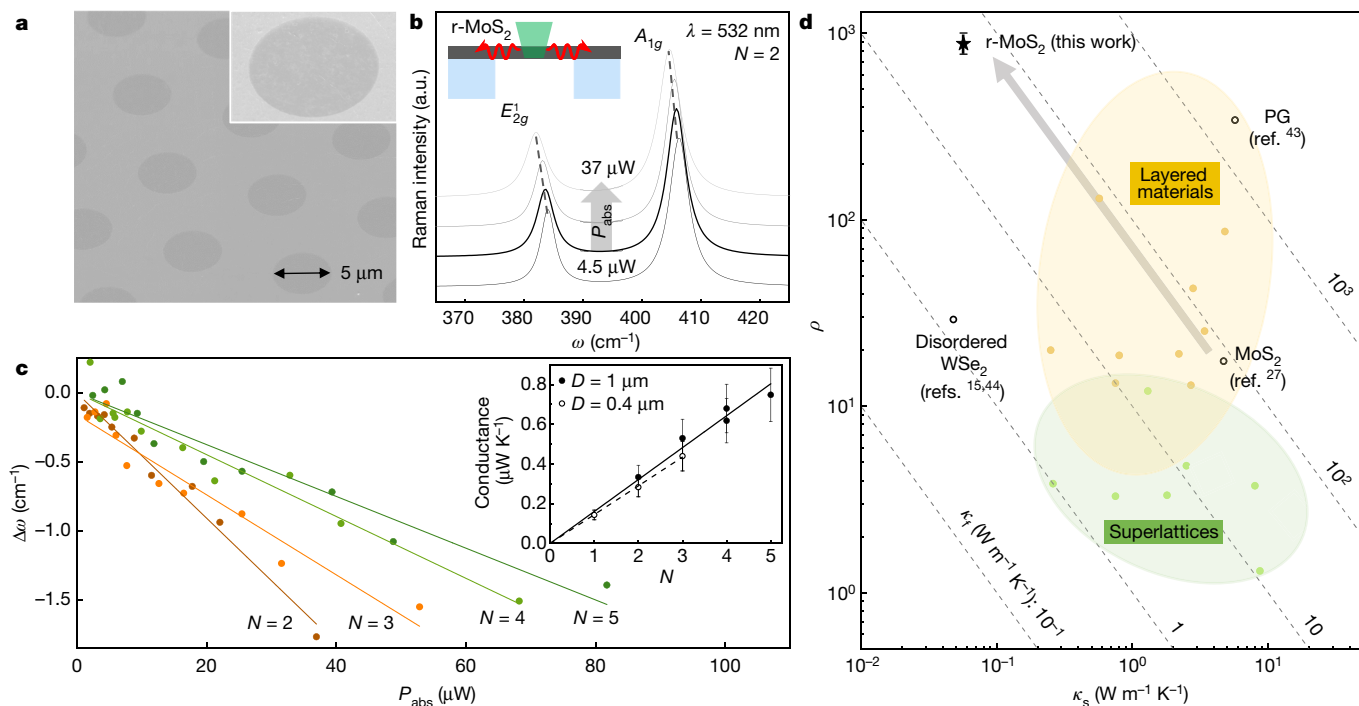


Fig. 3 | In-plane thermal properties and thermal anisotropy of r-MoS₂ films. **a**, 45° SEM micrograph of an $N = 4$ r-MoS₂ film suspended on a TEM grid for Raman thermometry. **b**, Raman spectra of an $N = 2$ r-MoS₂ film with different absorbed laser powers. Inset: Raman thermometry sample geometry. **c**, A_{1g} Raman peak shifts versus power absorbed by r-MoS₂ films of various N . Inset: layer-dependent thermal conductance values (absorbed power divided by temperature increase) in domain size $D = 1 \mu\text{m}$ and

$D = 400 \text{ nm}$ r-MoS₂ films. The error bars are the propagated uncertainties from the calculation of the conductance value for each N . **d**, Comparison of ρ (y axis), κ_x (x axis), and κ_r (diagonal dashed lines) measured for different anisotropic thermal conductors. r-MoS₂ has an ultrahigh ρ close to 900, which is larger than bulk MoS₂, PG, and disordered layered WSe₂. The error bar for ρ of r-MoS₂ comes from the propagated uncertainties of the calculated κ_{\perp} and κ_{\parallel} values.

thermal transport mechanism in-plane, in contrast to the glass-like thermal conduction along the through-plane direction.

Our experiments and calculations confirm that interlayer rotation in r-TMD films results in highly directional thermal conductivity and a direction-dependent thermal conduction mechanism. The rotation significantly reduces κ_{\perp} while maintaining high κ_{\parallel} , leading to an ultrahigh value of ρ . We estimate $\rho \approx 880 \pm 110$ at room temperature for the r-MoS₂ films, higher than that of pyrolytic graphite (PG), which is considered to be one of the most anisotropic thermal conductors ($\rho \approx 340$)⁴³. In Fig. 3d, we compare our result with other previously reported values of ρ in phonon-based solids^{15,27,43,44} (for a full comparison, see Extended Data Fig. 6b). Compared to a bulk MoS₂ crystal ($\rho \approx 20$)²⁷ or disordered layered WSe₂ ($\rho \approx 30$)^{15,44}, r-MoS₂ has a significantly larger ρ because interlayer rotation reduces only κ_{\perp} , as denoted by the grey arrow parallel to the equi- κ_r lines. This also suggests that ρ can be made even larger by starting with the monolayers of a layered vdW material with a higher κ_{\parallel} value such as graphene.

Anisotropic vdW heat diffuser

In Fig. 4, we show that the extreme anisotropy of our r-MoS₂ films can lead to excellent heat dissipation in-plane from a heat source and drastic thermal insulation in the through-plane direction. Using the COMSOL software, we perform thermal finite-element simulations of a 10-nm-thick r-MoS₂ film draped over a nanoscale Au electrode (15 nm tall, 100 nm wide) on a 50 nm SiO₂/Si substrate (Fig. 4a). Our simulation results show that for a fixed power of 8 mW supplied to the Au electrode (near thermal breakdown), the temperature rise ΔT of the Au electrode covered by r-MoS₂ is 50 K lower than that of the bare electrode, thereby demonstrating our film's effectiveness at spreading heat due to its excellent κ_{\parallel} (Fig. 4b, c). Interestingly, the extreme thermal anisotropy of our r-MoS₂ films provides thermal insulation in the through-plane direction,

with much lower MoS₂ surface ΔT values that are only one-third of the value of the bare Au electrode. While single-crystal MoS₂ displays similar properties, the insulation effect is stronger in r-MoS₂ (Extended Data Fig. 7a). This implies that heat is efficiently directed away from the hot Au electrode laterally through r-MoS₂ but not to the surface of r-MoS₂, making the surface of the entire device significantly cooler.

Our experiments corroborate these simulation results. For this, we fabricate nanoscale Au electrodes with the same geometry and substrate as in our simulation (image shown in Fig. 4d, inset) and transfer $N = 16$ r-MoS₂ (~10 nm thick) using the vacuum stacking process. Both bare and coated Au electrodes show similar resistance at low currents. At higher currents, current-induced Joule heating leads to the thermally activated electromigration process, which causes the electrodes to fail⁴⁵. Figure 4d compares representative current–voltage (I – V) curves measured from a bare and coated Au electrode, which shows that the Au electrode with r-MoS₂ can carry a larger current without breaking. The histogram of critical current I_c (maximum current a Au electrode sustains for at least 20 s) measured from 20 electrodes (10 bare and 10 with r-MoS₂) reveals a ~50% increase in the median I_c values (Fig. 4e). These results demonstrate our r-MoS₂ film's ability to efficiently dissipate Joule heat and keep the electrodes cool, as our simulation predicts. As the electromigration process is dominated by the temperature, the observed increase of I_c and maximum power before breaking is in good agreement with our simulation in Fig. 4c. Furthermore, we note that the r-MoS₂ film can be integrated with the Au electrodes using mild conditions that do not affect their electrical properties (Extended Data Fig. 7b).

Outlook

We expect interlayer rotation to be an effective and generalizable way to reduce κ_{\perp} and potentially engineer anisotropic thermal properties

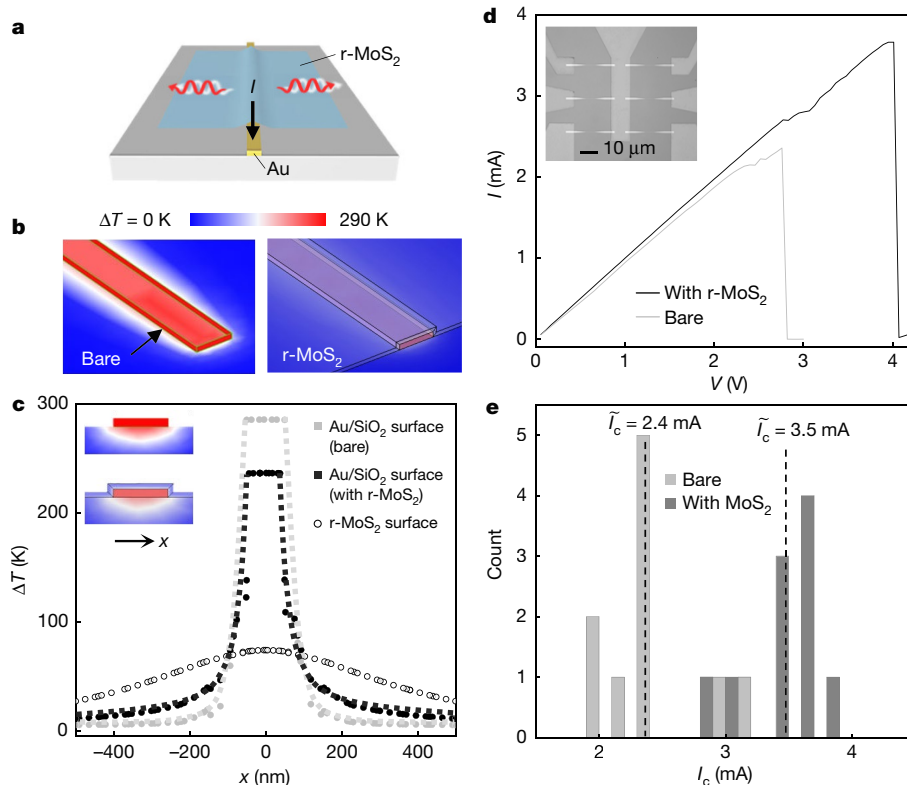


Fig. 4 | Temperature profiles and heat spreader efficiencies of r-MoS₂ films on Au electrodes. **a**, Schematic of the sample configuration of r-MoS₂ draped across a current-carrying Au electrode that is 100 nm wide, 15 nm thick and 10 μm long. **b**, Thermal finite element modelling results of Au electrodes (bare, covered with 10-nm-thick r-MoS₂) at constant heating power of 8 mW supplied through Joule heating. **c**, Lateral profiles of temperature increases across the

Au/SiO₂ surface (solid dots) and on the r-MoS₂ top surface (open circles). Insets: cross-sectional temperature distribution of Au electrodes with and without r-MoS₂, using the same colour scale as in **b**. **d**, I - V curve of an Au electrode, with and without $N = 16$ r-MoS₂. Inset: optical micrograph of six fabricated Au electrodes. **e**, Histogram of I_c of Au electrodes with and without an $N = 16$ r-MoS₂ heat spreader and their median values.

in a variety of layered materials. Our results call for a systematic study of the exact relation between κ_{\perp} and rotation angle, which could reveal unexpected relationships analogous to the studies of electrical transport in twisted bilayer graphene⁴⁶. Interlayer rotations can be combined with other parameters (such as pressure or interlayer spacing^{47,48}) and advanced structures (superlattices and heterostructures¹⁸) to realize highly tunable ρ , allowing for the customization of thermal transport properties with an unprecedented level of directional and spatial control.

Online content

Any methods, additional references, Nature Research reporting summaries, source data, extended data, supplementary information, acknowledgements, peer review information; details of author contributions and competing interests; and statements of data and code availability are available at <https://doi.org/10.1038/s41586-021-03867-8>.

- Minnich, A. J. Exploring the extremes of heat conduction in anisotropic materials. *Nanoscale Microscale Thermophys. Eng.* **20**, 1–21 (2016).
- Cui, Y., Li, M. & Hu, Y. Emerging interface materials for electronics thermal management: experiments, modeling, and new opportunities. *J. Mater. Chem. C* **8**, 10568–10586 (2020).
- Moore, A. L. & Shi, L. Emerging challenges and materials for thermal management of electronics. *Mater. Today* **17**, 163–174 (2014).
- Norley, J., Tzeng, J. J.-W., Getz, G., Klug, J. & Fedor, B. The development of a natural graphite heat-spreader. In *Seventeenth Annual IEEE Semiconductor Thermal Measurement and Management Symposium* 107–110 (IEEE, 2001).
- Chung, D. D. L. & Takizawa, Y. Performance of isotropic and anisotropic heat spreaders. *J. Electron. Mater.* **41**, 2580–2587 (2012).
- Termentzidis, K. Thermal conductivity anisotropy in nanostructures and nanostructured materials. *J. Phys. Appl. Phys.* **51**, 094003 (2018).

- Lee, S.-M., Cahill, D. G. & Venkatasubramanian, R. Thermal conductivity of Si–Ge superlattices. *Appl. Phys. Lett.* **70**, 2957–2959 (1997).
- Luckyanova, M. N. et al. Anisotropy of the thermal conductivity in GaAs/AlAs superlattices. *Nano Lett.* **13**, 3973–3977 (2013).
- Borca-Tasciuc, T. et al. Thermal conductivity of symmetrically strained Si/Ge superlattices. *Superlattices Microstruct.* **28**, 199–206 (2000).
- Lee, W.-Y. et al. Anisotropic temperature-dependent thermal conductivity by an Al₂O₃ interlayer in Al₂O₃/ZnO superlattice films. *Nanotechnology* **28**, 105401 (2017).
- Rawat, V., Koh, Y. K., Cahill, D. G. & Sands, T. D. Thermal conductivity of (Zr,W)/N/ScN metal/semiconductor multilayers and superlattices. *J. Appl. Phys.* **105**, 024909 (2009).
- Sun, B. et al. Dislocation-induced thermal transport anisotropy in single-crystal group-III nitride films. *Nat. Mater.* **18**, 136–140 (2019).
- Jiang, P., Qian, X., Yang, R. & Lindsay, L. Anisotropic thermal transport in bulk hexagonal boron nitride. *Phys. Rev. Mater.* **2**, 04005 (2018).
- Chiritescu, C. et al. Low thermal conductivity in nanoscale layered materials synthesized by the method of modulated elemental reactants. *J. Appl. Phys.* **104**, 033533 (2008).
- Chiritescu, C. et al. Ultralow thermal conductivity in disordered, layered WSe₂ crystals. *Science* **315**, 351–353 (2007).
- Hadland, E. C. et al. Ultralow thermal conductivity of turbostratically disordered MoSe₂ ultra-thin films and implications for heterostructures. *Nanotechnology* **30**, 285401 (2019).
- Hadland, E. et al. Synthesis, characterization, and ultralow thermal conductivity of a lattice-mismatched SnSe₂(MoSe₂)_{1.32} heterostructure. *Chem. Mater.* **31**, 5699–5705 (2019).
- Vaziri, S. et al. Ultrahigh thermal isolation across heterogeneously layered two-dimensional materials. *Sci. Adv.* **5**, eaax1325 (2019).
- Kang, K. et al. High-mobility three-atom-thick semiconducting films with wafer-scale homogeneity. *Nature* **520**, 656–660 (2015).
- Kang, K. et al. Layer-by-layer assembly of two-dimensional materials into wafer-scale heterostructures. *Nature* **550**, 229–233 (2017).
- Liu, K. et al. Evolution of interlayer coupling in twisted molybdenum disulfide bilayers. *Nat. Commun.* **5**, 4966 (2014).
- Sood, A. et al. Quasi-ballistic thermal transport across MoS₂ thin films. *Nano Lett.* **19**, 2434–2442 (2019).
- Li, Z. et al. Size dependence and ballistic limits of thermal transport in anisotropic layered two-dimensional materials. Preprint at *arXiv* <https://arxiv.org/abs/1711.02772> (2017).

24. Schauble, K. et al. Uncovering the effects of metal contacts on monolayer MoS₂. *ACS Nano* **14**, 14798–14808 (2020).
25. Liu, Y. et al. Approaching the Schottky–Mott limit in van der Waals metal–semiconductor junctions. *Nature* **557**, 696–700 (2018).
26. Liu, J., Choi, G.-M. & Cahill, D. G. Measurement of the anisotropic thermal conductivity of molybdenum disulfide by the time-resolved magneto-optic Kerr effect. *J. Appl. Phys.* **116**, 233107 (2014).
27. Jiang, P., Qian, X., Gu, X. & Yang, R. Probing anisotropic thermal conductivity of transition metal dichalcogenides MX₂ (M=Mo, W and X=S, Se) using time-domain thermoreflectance. *Adv. Mater.* **29**, 1701068 (2017).
28. Evans, D. J. Homogeneous NEMD algorithm for thermal conductivity—application of non-canonical linear response theory. *Phys. Lett. A* **91**, 457–460 (1982).
29. Fan, Z., Chen, W., Vierimaa, V. & Harju, A. Efficient molecular dynamics simulations with many-body potentials on graphics processing units. *Comput. Phys. Commun.* **218**, 10–16 (2017).
30. Xu, K. et al. Thermal transport in MoS₂ from molecular dynamics using different empirical potentials. *Phys. Rev. B* **99**, 054303 (2019).
31. Li, D., Schleife, A., Cahill, D. G., Mitchson, G. & Johnson, D. C. Ultralow shear modulus of incommensurate [SnSe]_n[MoSe₂]_n layers synthesized by the method of modulated elemental reactants. *Phys. Rev. Mater.* **3**, 043607 (2019).
32. Huang, S. et al. Probing the interlayer coupling of twisted bilayer MoS₂ using photoluminescence spectroscopy. *Nano Lett.* **14**, 5500–5508 (2014).
33. Erhart, P., Hyldgaard, P. & Lindroth, D. O. Microscopic origin of thermal conductivity reduction in disordered van der Waals solids. *Chem. Mater.* **27**, 5511–5518 (2015).
34. Yan, R. et al. Thermal conductivity of monolayer molybdenum disulfide obtained from temperature-dependent Raman spectroscopy. *ACS Nano* **8**, 986–993 (2014).
35. Sahoo, S., Gaur, A. P. S., Ahmadi, M., Guinel, M. J.-F. & Katiyar, R. S. Temperature-dependent Raman studies and thermal conductivity of few-layer MoS₂. *J. Phys. Chem. C* **117**, 9042–9047 (2013).
36. Zhang, X. et al. Measurement of lateral and interfacial thermal conductivity of single- and bilayer MoS₂ and MoSe₂ using refined optothermal Raman technique. *ACS Appl. Mater. Interfaces* **7**, 25923–25929 (2015).
37. Taube, A., Judek, J., Łapińska, A. & Zdrojek, M. Temperature-dependent thermal properties of supported MoS₂ monolayers. *ACS Appl. Mater. Interfaces* **7**, 5061–5065 (2015).
38. Lindroth, D. O. & Erhart, P. Thermal transport in van der Waals solids from first-principles calculations. *Phys. Rev. B* **94**, 115205 (2016).
39. Jo, I., Pettes, M. T., Ou, E., Wu, W. & Shi, L. Basal-plane thermal conductivity of few-layer molybdenum disulfide. *Appl. Phys. Lett.* **104**, 201902 (2014).
40. Wei, X. et al. Phonon thermal conductivity of monolayer MoS₂: a comparison with single layer graphene. *Appl. Phys. Lett.* **105**, 103902 (2014).
41. Cai, Y., Lan, J., Zhang, G. & Zhang, Y.-W. Lattice vibrational modes and phonon thermal conductivity of monolayer MoS₂. *Phys. Rev. B* **89**, 035438 (2014).
42. Liu, X., Zhang, G., Pei, Q.-X. & Zhang, Y.-W. Phonon thermal conductivity of monolayer MoS₂ sheet and nanoribbons. *Appl. Phys. Lett.* **103**, 133113 (2013).
43. Ho, C. Y., Powell, R. W. & Liley, P. E. Thermal conductivity of the elements. *J. Phys. Chem. Ref. Data* **1**, 279–421 (1972).
44. Mavrokefalos, A., Nguyen, N. T., Pettes, M. T., Johnson, D. C. & Shi, L. In-plane thermal conductivity of disordered layered WSe₂ and (W)_n(WSe₂)_n superlattice films. *Appl. Phys. Lett.* **91**, 171912 (2007).
45. Ho, P. & Kwok, T. Electromigration in metals. *Rep. Prog. Phys.* **52**, 301–348 (1989).
46. Cao, Y. et al. Unconventional superconductivity in magic-angle graphene superlattices. *Nature* **556**, 43–50 (2018).
47. Sood, A. et al. An electrochemical thermal transistor. *Nat. Commun.* **9**, 4510 (2018).
48. Chen, S., Sood, A., Pop, E., Goodson, K. E. & Donadio, D. Strongly tunable anisotropic thermal transport in MoS₂ by strain and lithium intercalation: first-principles calculations. *2D Mater.* **6**, 025033 (2019).

Publisher's note Springer Nature remains neutral with regard to jurisdictional claims in published maps and institutional affiliations.



Open Access This article is licensed under a Creative Commons Attribution 4.0 International License, which permits use, sharing, adaptation, distribution and reproduction in any medium or format, as long as you give appropriate credit to the original author(s) and the source, provide a link to the Creative Commons license, and indicate if changes were made. The images or other third party material in this article are included in the article's Creative Commons license, unless indicated otherwise in a credit line to the material. If material is not included in the article's Creative Commons license and your intended use is not permitted by statutory regulation or exceeds the permitted use, you will need to obtain permission directly from the copyright holder. To view a copy of this license, visit <http://creativecommons.org/licenses/by/4.0/>.

© The Author(s) 2021

Methods

Sample preparation

Large-area, polycrystalline transition metal dichalcogenide (TMD) (MoS_2 and WS_2) monolayers were grown on SiO_2/Si substrates in a hot-walled tube furnace via metal-organic chemical vapour deposition adapted from a previously reported protocol¹⁹. The growth conditions were optimized to produce high-quality monolayer materials with structural characteristics necessary for thermal measurements. These characteristics include large domain size ($D \approx 1 \mu\text{m}$ and $0.4 \mu\text{m}$), full monolayer coverage, and laterally stitched grain boundaries.

Briefly, $\text{Mo}(\text{CO})_6$ and $\text{W}(\text{CO})_6$ (diluted in N_2 to 15 torr) were used as the metal precursors for the MoS_2 and WS_2 growths, respectively. $(\text{C}_2\text{H}_5)_2\text{S}$ was used as the chalcogen source. All precursors were kept at room temperature. N_2 and H_2 were used as carrier gases. Typical growth times were 15–20 h for MoS_2 at a growth temperature of 525 °C. Typical growth times for WS_2 were 2 h at a temperature of 650 °C.

To make the r-TMD films, a TMD monolayer was spin-coated with PMMA A8 (poly-methyl methacrylate, 495 K, 4% diluted in anisole) at 2,800 rpm for 60 s, then baked at 180 °C for 3 min. The PMMA-coated monolayer was stacked onto TMD monolayers layer by layer to a target layer number (N) and transferred to the desired substrates using a previously reported programmed vacuum stacking method²⁰.

TDTR samples. The stacked r-TMD films were transferred onto sapphire substrates (Valley Design, C-plane), which were cleaned with Nanostrip solution for 20 min at 60 °C and then rinsed with deionized water. The PMMA layer on the film was removed by immersing the entire substrate in acetone at 60 °C for 1 h. The film was annealed under a 400/100 SCCM Ar/H_2 environment at 350 °C for 4 h. After cleaning, ~90-nm-thick, $90 \mu\text{m} \times 90 \mu\text{m}$ Al pads were deposited onto the TMD films through a holey TEM grid shadow mask using electron-beam evaporation.

Raman thermometry samples. Raman experiments were performed on a different set of films from the TDTR-measured films. First, holey SiN_x transmission electron microscopy (TEM) grids were cleaned in a N_2/H_2 plasma at 100 °C and 180 mtorr for 3 min, followed by the transfer of stacked MoS_2 films onto the TEM grids. During the transfer process, the PMMA-coated r- MoS_2 was suspended on holey thermal release tape before contacting the TEM grid. The extra PMMA- MoS_2 not on the TEM grid was cut away at 180 °C so the PMMA layer was softened. PMMA was removed from r- MoS_2 on the TEM grid via annealing the film in 400/100 SCCM Ar/H_2 at 350 °C for 4 h.

Cross-sectional STEM

The $N = 10$ films were coated with Al that was electron beam evaporated onto the surface, whereas the top surface of $N = 20$ films was bare. The r- MoS_2 cross-section was prepared using a Thermo Scientific Strata 400 focused ion beam. Protective layers of carbon (~200 nm) and platinum (~1 μm) were deposited on the sample. A cross-section was milled at a 90° angle from the sample using a Ga ion beam at 30 kV. The cross-section was then polished to ~150 nm thickness with the ion beam at 5 kV.

The cross-section was imaged in a Thermo Scientific Titan Themis scanning transmission electron microscope at 120 kV with a probe convergence angle of 21.4 mrad. The $N = 10$ film was imaged at a beam voltage of 120 kV, whereas the $N = 20$ film was imaged at 300 kV. All images were analysed using the open-source software Cornell Spectrum Imager⁴⁹. The high-angle annular dark field (HAADF) image of the sample (see 'TMD films with interlayer rotation' in the main text; Fig. 1d) shows, from top to bottom, the Al crystal lattice along the [110] zone axis, ten layers of MoS_2 (bright bands), followed by an AlO_x layer.

TDTR

We used TDTR to measure the thermal conductivity of our r-TMD films. We used a mode-locked Ti:sapphire laser, which produced a train of

pulses at a repetition rate of 74.86 MHz, with wavelength centred at 785 nm and a total power of 18 mW. The steady-state temperature rise at the surface of the samples was <4 K for all temperatures. For the low temperature TDTR measurements, an INSTEC stage was used with liquid nitrogen cooling; the other beam conditions were the same. The laser beam was split into pump and probe beams. A mechanical delay stage was used to delay the arrival of the probe with respect to the pump on the sample surface by changing their optical path difference, before they were focused onto the sample surface through an objective lens. The $1/e^2$ radius of the focused laser beams was 10.7 μm . For our measurements, we modulated the pump beam at a frequency of 9.3 MHz so that the thermoreflectance change at the sample surface could be detected by the probe beam through lock-in detection. The ratio of the in-phase and out-of-phase signals from the lock-in was fitted to a thermal diffusion model. The full details of the TDTR measurement can be found elsewhere^{50,51}.

Calculation of κ_{\perp} . The modelling required material parameters such as heat capacity (C), thickness (h), interface conductance (G) and thermal conductivity (κ) for each layer. Our TDTR samples have three chemically distinct layers with the following structure (from the top): Al/r-TMD/sapphire. In our fitting process, the heat capacities of all materials were adopted from literature⁵². The thickness of Al layer was obtained from picosecond acoustics using a longitudinal speed of sound of 6.42 nm ps⁻¹ (Extended Data Fig. 3e). The thickness of the r-TMD film was calculated from the product of N and the interlayer spacing (d). The latter was measured by performing grazing-incidence wide-angle X-ray spectroscopy (GIWAXS; see GIWAXS section below in the Methods and Extended Data Fig. 2) on the r-TMD films, which gave $d \approx 0.64$ nm. The total thicknesses of the r- MoS_2 films were <15 nm; thus, this layer was treated as part of the Al-sapphire interface as a single thermal layer characterized by a single thermal conductance value G_{\perp} . We used the bulk value of the volumetric heat capacity of 1.89 J K⁻¹ cm⁻³ for the r- MoS_2 layer. The thermal conductivity of the Al layer was calculated from the Wiedemann–Franz law using the electrical resistance of a transducer layer deposited on a bare sapphire substrate as a reference sample. The thermal conductivity of the sapphire substrate, 35 W m⁻¹ K⁻¹, was measured using the same reference sample. Thus, the only remaining free parameter to fit for was G_{\perp} . To obtain κ_{TMD} from G_{\perp} , we perform TDTR on various N -layer TMD films, then perform a linear fit on the effective thermal resistance (R_{TDTR} , equal to $1/G_{\perp}$) versus N data points; the slope of the linear fit is inversely proportional to the thermal conductivity, whereas the y-intercept yields the total interfacial thermal resistances (R_0) of the top and bottom interfaces. In Extended Data Table 1, our R_0 values match the values reported in literature^{22,27,53}. We note that, although R_0 changes depending on the chemical nature of the metal–TMD interface, the slope of the $R_{\text{TDTR}}-N$ plot (which is used to extract κ_{\perp}) remains constant, despite the use of different transducer metals, as illustrated in Extended Data Fig. 3d.

For highly anisotropic materials, the anisotropy ratio of an in-plane thermal conductivity to a through-plane conductivity should be included in the thermal model. Despite the ultrahigh thermal anisotropy expected of our r-TMD films, our through-plane thermal conductivity measurements were probably not sensitive to the thermal conductivity anisotropy given the thinness of our r-TMD films. Hence, we assumed a one-dimensional thermal transport model and neglected the in-plane thermal transport in our calculations. We found that the effect of the anisotropy was significant only at a smaller modulation frequency ($f = 1.12$ MHz) and $1/e^2$ beam radius of ~3.2 μm , and so we deliberately chose a larger f and a $1/e^2$ beam radius to reduce the sensitivity of our TDTR signal to the in-plane thermal transport.

Raman thermometry

We followed a similar procedure from previous reports^{34,54,55} with the modification of lower pressures during measurement. All the Raman measurements were performed using a Horiba Raman spectrometer with a laser excitation wavelength of 532 nm and a long-working

distance, 50× objective lens (numerical aperture (NA) = 0.5). The r-MoS₂ A_{1g} peak shift (ω) versus temperature (T) relation was calibrated using a temperature-controlled, low-vacuum-compatible Linkam stage. For all our Raman measurements, we used the A_{1g} peak since this out-of-plane vibrational mode is less sensitive to in-plane strain⁵⁶. The ω - T calibration measurements were performed at atmospheric pressure and with low laser powers. The stage was purged with dry N₂ gas throughout the calibration step to prevent oxidative damage to the film at high temperatures. Extended Data Fig. 5d shows representative ω - T calibration curves for $N = 2$ and $N = 4$ r-MoS₂ films, where a linear fit was performed to obtain the temperature-dependent Raman coefficients. This process was repeated for r-MoS₂ films with different domain sizes D (400 nm and 1 μ m) for $N = 1$ –3 (Extended Data Fig. 5e).

To measure the in-plane thermal conductivity ($\kappa_{||}$) of our films, the laser power (P) was varied and the corresponding $\Delta\omega$ values were recorded. The in-plane thermal conductance was obtained from the reciprocal of the slope of the $\Delta\omega$ - P linear fit, which is illustrated for r-MoS₂ films with $N = 2$ –5 and $D = 1$ μ m in Fig. 3c and for r-MoS₂ films with $N = 1$ –3 and $D = 400$ nm in Extended Data Fig. 5b. As thermal conductivity changes with temperature, laser powers were kept below 250 μ W to induce a relatively small ΔT in the film and ensure that the value of $\kappa_{||}$ remained relatively constant. This was verified from the observation of a linear $\Delta\omega$ - P regime for $P < 250$ μ W. Any higher laser powers caused the $\Delta\omega$ - P curve to deviate from the linear regime with $\frac{d^2\omega}{dP^2} < 0$. This indicates that the local film temperature increased faster at higher $P > 250$ μ W, which signified that the thermal conductivity could no longer be assumed to be constant. Instead, the thermal conductivity decreased with increasing temperature, consistent with the T -dependent Raman measurements.

The $\Delta\omega$ - P measurements were conducted at a pressure of 15 torr to eliminate any heat loss to air. We verified that a lower pressure down to 4 mtorr gave rise to similar $\Delta\omega$ values as the measurements at 15 torr (Extended Data Fig. 5a), weighted by the beam spot size.

The other relevant input quantities for our thermal calculations were obtained as follows: the beam spot radius (r_0) was estimated using the knife-edge method, whereby a one-dimensional Raman map was taken across a gold step edge on an Au-patterned silicon chip, and the spatial distribution of the integrated peak intensities was fitted to an error function. We measured $r_0 = 0.71 \pm 0.09$ μ m. The laser powers were measured using a Thorlabs standard silicon photodiode power sensor. The r-MoS₂ absorbance $A = \frac{\text{Absorbed light intensity}}{\text{Incident light intensity}}$ was measured at room temperature on a white-light microscope with a 532 nm band-pass filter and a low-NA condenser aperture. We measured the light intensity transmitted through and reflected from a r-MoS₂ film suspended on a TEM grid, then compared it against a blank TEM grid. The data were collected using a 12-bit SensiCam QE CCD camera. The pixel intensities were analysed using ImageJ. The values for A were calculated using the formula $A = 1 - T - R$. We measured $A(N)$ for $N = 1$ –5, then fitted A to a power law. $A(N)$ was found to follow the relation $A = 1 - 0.92^N$ (Extended Data Fig. 5c), which matched previous reports²⁰. We use the value A measured at room temperature for our Raman analysis.

Calculation of $\kappa_{||}$. To obtain the value of $\kappa_{||}$, we used the two-dimensional thermal diffusion equation with a radial symmetry, following previous reports of Raman thermometry of two-dimensional films^{54,55}. We assumed a Gaussian laser profile $q(r) = \frac{PA}{(\pi r_0^2)t} \exp\left(-\frac{r^2}{r_0^2}\right)$. We solved for $\kappa_{||}$ numerically using the following equations:

$$\kappa_{||} \frac{1}{r} \frac{d}{dr} \left(r \frac{dT_{\text{susp}}(r)}{dr} \right) + q(r) = 0; r < R$$

$$\kappa_{||} \frac{1}{r} \frac{d}{dr} \left(r \frac{dT_{\text{supp}}(r)}{dr} \right) - \frac{G}{t} [T_{\text{supp}}(r) - T_a] = 0; r > R$$

applying the boundary conditions

$$T_{\text{susp}}(R) = T_{\text{supp}}(R)$$

$$\frac{dT_{\text{susp}}}{dr}(R) = \frac{dT_{\text{supp}}}{dr}(R)$$

where r is the distance from TEM hole centre, P is the laser power, t is the film thickness, R is the TEM hole radius, T is the film temperature where $T_{\text{susp}}, r \leq R$ and $T_{\text{supp}}, r \geq R$, T_a is the ambient temperature, A is the fraction of laser power absorbed, and $G = 10$ MW m⁻² K⁻¹ is the interfacial thermal conductance between r-MoS₂ and SiN_x.

We solved for the expression of $T(r)$ and obtained an expression for the average temperature measured by the Raman shift

$$T_m = \frac{\int_0^R T(r) r \times \exp\left(-\frac{r^2}{r_0^2}\right) dr}{\int_0^R r \times \exp\left(-\frac{r^2}{r_0^2}\right) dr}$$

$\kappa_{||}$ was obtained by substituting the experimentally measured value for T_m and solving the above equation numerically for $\kappa_{||}$. We calculated $\kappa_{||}$ for each N , and we reported the average value in the main text.

The total measurement uncertainty reported in the main text was calculated based on the error assessment for individual parameters. We used an approximate analytical solution

$$\Delta T = T_m - T_a \approx - \left(\frac{P_{\text{abs}}}{\kappa_{||}} \right) \left(\frac{1}{2\pi r t} \right) \ln \left(\frac{R}{r_0} \right)$$

$$\kappa_{||} \approx \left(\left(\frac{\Delta\omega}{\Delta P} \right)^{-1} \left(\frac{\Delta\omega}{\Delta T} \right) \right) \left(\frac{A_0}{2\pi d} \right) \ln \left(\frac{R}{r_0} \right)$$

where ω is the Raman frequency of A_{1g} peak, A_0 is the absorption of the monolayer, and d is the thickness of a monolayer. The difference between the full numerical solution and this analytical form is below 3%. We identified the following independent quantities that carry uncertainty for consideration in our overall uncertainty estimation of $\kappa_{||}$.

1. $\frac{\Delta P}{\Delta T} = \left(\frac{\Delta\omega}{\Delta P} \right)^{-1} \left(\frac{\Delta\omega}{\Delta T} \right)$: the associated uncertainty was derived from the error in the linear fit of $\left(\frac{\Delta\omega}{\Delta P} \right)$ and $\left(\frac{\Delta\omega}{\Delta T} \right)$ for every sample measured.

The total uncertainty in the average $\frac{\Delta P}{\Delta T}$ value was 9% for $D = 1$ μ m and 8% for $D = 400$ nm.

2. $\left(\frac{A_0}{2\pi d_0} \right)$: the uncertainty in A_0 from the $A(N)$ fit was 4%.

3. $\ln\left(\frac{R}{r_0}\right)$: the uncertainty originated from the uncertainty in r_0 . From 14 repeated measurements of the beam spot size using the knife-edge method, we calculated the standard deviation of r_0 to be 12%, which translated to an uncertainty in the expression $\ln\left(\frac{R}{r_0}\right)$ to be 9%.

Total uncertainty in $\kappa_{||}$: 13% (for both $D = 1$ μ m and $D = 400$ nm).

Variable pressure Raman thermometry measurements. Previous Raman thermometry measurements on graphene films⁵⁷ and carbon nanotubes⁵⁸ had shown an appreciable difference between measurements performed in air and at lower pressures, as well as in different gaseous environments. We extended the same precaution and repeated our Raman thermometry measurements at low pressures to reduce heat dissipation to air, an extra heat loss channel that would lead to an overestimation of the thermal conductivity of the r-MoS₂ films.

Our $\Delta\omega$ - P measurements in Fig. 3 were conducted at a pressure of 15 torr. In Extended Data Fig. 5a, we compared the $\Delta\omega$ values of $N = 2$ r-MoS₂ at three different P (1 atm, 15 torr and 4 mtorr), after correcting for the different laser spot sizes.

Temperature-dependent Raman thermometry for $\kappa_{||}$. We performed Raman thermometry while varying the ambient temperature T_a using a Linkam stage. No oxidation or sample damage was detected for any of the temperatures used. We performed the same $\Delta\omega$ - P measurements and calculated the $\kappa_{||}$ value of for each T_a . We plot a $\kappa_{||}$ versus T curve, where the x axis is $T = T_a$ (Extended Data Fig. 6a).

We note that the measured values of $\kappa_{||}$ here were lower than the room temperature values reported in the main text. We ascribe this to the sub-optimal growth conditions for the constituent monolayers used for this sample.

r-MoS₂ heat spreader experiments (electromigration of Au nanoelectrodes)

All Au electrodes were fabricated on Si substrates with 50 nm dry SiO₂ in three nanopatterning and deposition layers: (A) the nanoelectrodes (10 μ m long, 100 nm wide, 15 nm thick); (B) the contact pads that would interface with the external electronics (200 μ m long, 300 μ m wide, 100 nm thick); and (C) the leads connecting the nanoelectrodes and the contact pads (~1,000 μ m long, 50 μ m wide, 15 nm thick).

We first defined the leads (B) and then the contact pads (C) using standard photolithography, and electron-beam evaporation of Ti (1 nm)/Au and lift-off. The final step was defining the nanoelectrodes (A) using electron-beam lithography, deposition of 15 nm Au, and lift-off.

Electron-beam lithography. We used a bilayer of resists: copolymer P(MMA-MAA 11%) in ethyl lactate and 950 K PMMA A4. The writing was executed with a Raith EBPG 5000 Plus E-beam writer with the beam conditions of 25 nA current, dose of 1,200 μ C cm⁻², 300 μ m aperture size, 100 kV accelerating voltage.

Film transfer. After the nanoelectrodes, leads and pads were fabricated, the device was cleaned with an O₂ plasma for 30 s to remove any resist residue and to promote adhesion of the r-MoS₂ film to the Au electrodes and the SiO₂ surface. A PMMA coated $N = 16$ r-MoS₂ film was transferred onto the electrodes using the same process as the stacking method as outlined above. The PMMA on the r-MoS₂ film was removed by immersing the entire chip in toluene at 60 °C for 1 h.

Electrical measurements. All measurements were performed in ambient conditions with a home-built probe station in a two-probe geometry. To measure I_c in Fig. 4d, we swept the voltage bias in only one direction at a rate such that the rate in current increase is 0.05 mA per 20 s.

For comparison, we deposited SiN_x onto Au electrodes (10 μ m long, 10 nm thick, 100 nm wide) using plasma-enhanced chemical vapour deposition with the following conditions: 10 s deposition at 90 °C and 10 torr and 1,000 W plasma power, with 25 SCCM/35 SCCM SiH₄ and N₂ as the precursors. The film thickness was measured via ellipsometry to be 16 nm.

Computational methodology

Structural models. Structural models were created according to an algorithm previously described in literature⁵⁹, which was implemented in Python using the atomic simulation environment package⁶⁰. The structural models were subsequently relaxed using an analytic bond-order potential⁶¹ and implemented in the LAMMPS package⁶².

The main r-MoS₂ model used in the simulations described here comprised 10 randomly stacked layers with a total of 10,152 atoms. The 10 layers came in pairs; each pair was related by a 60° rotation. The four primitive angles present in the stack are 16.1, 25.28, 34.72 and 43.9°. Due to strain, each layer contained a different number of atoms in accordance with strains of around 10%.

The bulk structure used in the MD simulations comprised 40 layers (20 conventional unit-cells) with a total of 26,880 atoms and cell vectors of 44.44, 43.98 and 243.57 Å.

HNEMD simulations. The interatomic potential in our simulations produces the expected slight increase in the interlayer spacing in r-MoS₂ and yields thermal conductivities and phonon dispersions of bulk MoS₂ that agree with previous experimental observations and Boltzmann transport calculations based on density functional theory³⁸, confirming our MD model's suitability for this study. The structures described above were driven by an optimized driving force (Extended Data Fig. 8a) and subsequently relaxed, after which the thermal conductivity was computed using HNEMD simulations⁶³ and implemented in the graphics processing units molecular dynamics (GPUMD) package²⁹. We also included the effects of thermal expansion in the simulations (Extended Data Fig. 8b). The calculated $\kappa_{||}$ values of r-MoS₂ are higher than the experimental values. We attribute the discrepancy to our neglecting any quantum effects and all boundary scattering in our simulations. Including such effects could further improve results from simulations. Statistics and averages were gathered from ten independent simulation runs for each system and temperature. The other parameters used in these simulations are compiled in Extended Data Table 2.

Phonon dispersion and lifetimes. We first generated the bulk MoS₂ phonon dispersion in the harmonic limit as a reference to phonon dispersion calculations using MD simulations. We computed the harmonic (0 K) phonon dispersion using the PHONOPY package⁶⁴. Forces were computed for $6 \times 6 \times 2$ supercells using the LAMMPS code. Lifetimes were calculated using the lowest applicable order of perturbation theory using the PHONO3PY package⁶⁵, which also provided us with the thermal conductivity as obtained from a direct solution of the Boltzmann transport equation⁶⁶. In these calculations, the Brillouin zone was sampled using a $10 \times 10 \times 10$ Γ -centred q-point mesh, which was chosen for consistency with the supercell used in the HNEMD simulations.

Next, we compared the dispersion of bulk MoS₂ to that calculated using MD simulations to verify the accuracy of our MD simulations for calculating the phonon dispersion of r-MoS₂. For both bulk and r-MoS₂, we extracted the phonon dispersions and lifetimes at 300 K by analysing the longitudinal and transverse current correlation functions generated by MD simulations in the microcanonical (NVE) ensemble using dynasor⁶⁷. The MD simulations details were otherwise identical to the HNEMD simulations. The obtained correlation functions were Fourier transformed and fitted to peak shape functions corresponding to (over)damped harmonic oscillators using the full expressions given in the dynasor paper⁶⁷ to obtain phonon frequencies and lifetimes.

Finite-element analysis. We used the COMSOL software to simulate the steady-state temperature distribution in a Au electrode on a SiO₂/Si substrate. Our geometry contains an Au electrode that is 100 nm wide, 15 nm thick, and 10 μ m long on a 50-nm-thick SiO₂ layer on a Si substrate. We layer a 10-nm-thick MoS₂ film onto the Au electrode and the SiO₂ layer. For the thermal anisotropy consideration, we define the thermal conductivity slow axis direction to always be perpendicular to the film's bottom surface in contact with the substrate or the Au electrode, including the Au electrode side walls.

We supply the Au electrode with 8 mW uniformly over the entire volume as the heat source, matching the power conditions at which the Au electrode fails in our experiments. As the boundary condition, we set the bottom surface on the Si substrate to be at 293.15 K. We also account for all the interfacial thermal resistances between heterogeneous surfaces in our calculations, which include r-MoS₂/Au, r-MoS₂/SiO₂, Au/SiO₂, SiO₂/Si (refs. ⁶⁸⁻⁷¹). All effects of radiation are neglected as they do not affect the temperature values in our simulations.

Low-frequency Raman measurements

The low-frequency Raman spectra of $N = 2, 3$ and 4 r-MoS₂ films, along with the spectrum for MoS₂, are shown in Extended Data Fig. 4a. From the layer-dependence of the peak positions, we assigned these to be

the breathing modes of MoS₂ (ref.⁷²). We did not observe any peaks corresponding to shear modes in r-MoS₂. Our findings agree with theoretical studies of low-frequency Raman modes of twisted MoS₂ bilayers, which showed that the shear mode peaks redshift to below the detection capabilities (2 cm⁻¹)⁷³. The positions of the breathing mode peaks of the r-MoS₂ films were close to those in exfoliated few layer MoS₂ (Extended Data Fig. 4b) as reported in literature^{72,74}. This observation agreed with our MD simulations that suggested that the transverse vibrational mode was suppressed by interlayer rotation, while the longitudinal vibrational mode was retained.

GIWAXS

The GIWAXS measurement was performed using SAXSLAB (XENOCSS)'s GANESHA (lab-source Cu K α , photon flux ~108 photons s⁻¹) to characterize the interlayer spacing of r-MoS₂ films. An $N = 10$ r-MoS₂ film was prepared on a SiO₂/Si substrate. The incidence angle of the X-ray beam was 0.2° and the integration time was ~60 s. Radially integrating the two-dimensional diffraction images along the out-of-plane direction produced the diffraction spectrum along the c axis shown in Extended Data Fig. 2.

The peak position of 14° corresponded to an interlayer spacing of 6.4 Å in the [0 0 1] direction, which matched previous reports of r-TMD films²⁰.

Data availability

The data that support the findings of this study are available from the corresponding authors on reasonable request. Source data are provided with this paper.

Code availability

All code used in this work is available from the corresponding authors on reasonable request.

49. Cueva, P., Hovden, R., Mundy, J. A., Xin, H. L. & Muller, D. A. Data processing for atomic resolution electron energy loss spectroscopy. *Microsc. Microanal.* **18**, 667–675 (2012).
50. Cahill, D. G. Analysis of heat flow in layered structures for time-domain thermoreflectance. *Rev. Sci. Instrum.* **75**, 5119–5122 (2004).
51. Liu, J. et al. Simultaneous measurement of thermal conductivity and heat capacity of bulk and thin film materials using frequency-dependent transient thermoreflectance method. *Rev. Sci. Instrum.* **84**, 034902 (2013).
52. Ditmars, D. A., Plint, C. A. & Shukla, R. C. Aluminum. I. Measurement of the relative enthalpy from 273 to 929 K and derivation of thermodynamic functions for Al(s) from 0 K to its melting point. *Int. J. Thermophys.* **6**, 499–515 (1985).
53. Yue, X. F. et al. Measurement of interfacial thermal conductance of few-layer MoS₂ supported on different substrates using Raman spectroscopy. *J. Appl. Phys.* **127**, 104301 (2020).
54. Lee, J.-U., Yoon, D., Kim, H., Lee, S. W. & Cheong, H. Thermal conductivity of suspended pristine graphene measured by Raman spectroscopy. *Phys. Rev. B* **83**, 081419 (2011).
55. Cai, W. et al. Thermal transport in suspended and supported monolayer graphene grown by chemical vapor deposition. *Nano Lett.* **10**, 1645–1651 (2010).
56. Wang, Y., Cong, C., Qiu, C. & Yu, T. Raman spectroscopy study of lattice vibration and crystallographic orientation of monolayer MoS₂ under uniaxial strain. *Small* **9**, 2857–2861 (2013).
57. Chen, S. et al. Raman measurements of thermal transport in suspended monolayer graphene of variable sizes in vacuum and gaseous environments. *ACS Nano* **5**, 321–328 (2011).
58. Hsu, I.-K., Pettes, M. T., Aykol, M., Shi, L. & Cronin, S. B. The effect of gas environment on electrical heating in suspended carbon nanotubes. *J. Appl. Phys.* **108**, 084307 (2010).
59. Hermann, K. Periodic overlayers and moiré patterns: theoretical studies of geometric properties. *J. Phys. Condens. Matter* **24**, 314210 (2012).
60. Hjorth Larsen, A. et al. The atomic simulation environment—a Python library for working with atoms. *J. Phys. Condens. Matter* **29**, 273002 (2017).

61. Liang, T., Phillpot, S. R. & Sinnott, S. B. Parametrization of a reactive many-body potential for Mo–S systems. *Phys. Rev. B* **79**, 245110 (2009).
62. Plimpton, S. Fast parallel algorithms for short-range molecular dynamics. *J. Comput. Phys.* **117**, 1–19 (1995).
63. Evans, D. J. Homogeneous NEMD algorithm for thermal conductivity—application of non-canonical linear response theory. *Phys. Lett. A* **91**, 457–460 (1982).
64. Togo, A. & Tanaka, I. First principles phonon calculations in materials science. *Scr. Mater.* **108**, 1–5 (2015).
65. Togo, A., Chaput, L. & Tanaka, I. Distributions of phonon lifetimes in Brillouin zones. *Phys. Rev. B* **91**, 094306 (2015).
66. Chaput, L. Direct solution to the linearized phonon Boltzmann equation. *Phys. Rev. Lett.* **110**, 265506 (2013).
67. Franssón, E., Slabjanja, M., Erhart, P. & Wahnström, G. DYNASOR—a tool for extracting dynamical structure factors and current correlation functions from molecular dynamics simulations. *Adv. Theory Simul.* **4**, 2000240 (2021).
68. Yalon, E. et al. Energy dissipation in monolayer MoS₂ electronics. *Nano Lett.* **17**, 3429–3433 (2017).
69. Freedy, K. M., Olson, D. H., Hopkins, P. E. & McDonnell, S. J. Titanium contacts to MoS₂ with interfacial oxide: interface chemistry and thermal transport. *Phys. Rev. Mater.* **3**, 104001 (2019).
70. Lombard, J., Detcheverry, F. & Merabia, S. Influence of the electron–phonon interfacial conductance on the thermal transport at metal/dielectric interfaces. *J. Phys. Condens. Matter* **27**, 015007 (2015).
71. Kimling, J., Philipp-Kobs, A., Jacobsohn, J., Oepen, H. P. & Cahill, D. G. Thermal conductance of interfaces with amorphous SiO₂ measured by time-resolved magneto-optic Kerr-effect thermometry. *Phys. Rev. B* **95**, 184305 (2017).
72. Zhao, Y. et al. Interlayer breathing and shear modes in few-trilayer MoS₂ and WSe₂. *Nano Lett.* **13**, 1007–1015 (2013).
73. Huang, S. et al. Low-frequency interlayer Raman modes to probe interface of twisted bilayer MoS₂. *Nano Lett.* **16**, 1435–1444 (2016).
74. Zhang, X. et al. Raman spectroscopy of shear and layer breathing modes in multilayer MoS₂. *Phys. Rev. B* **87**, 115413 (2013).

Acknowledgements We thank D. F. Ogletree, J. Jureller, A. J. Mannix, J.-U. Lee, K.-H. Lee and M. Lee for their helpful discussions. We also acknowledge J.-H. Kang, A. Ye and C. Liang for their help with materials preparation. Primary funding for this work comes from Air Force Office of Scientific Research MURI projects (FA9550-18-1-0480 and FA9550-16-1-0031). Material growths done by F.M. and C.P. are partially supported by the University of Chicago MRSEC (NSF DMR-2011854) and Samsung Advanced Institute of Technology. This work makes use of the characterization facilities of the University of Chicago MRSEC (NSF DMR-2011854) and the Pritzker Nanofabrication Facility at the University of Chicago, which receives support from SHYNE Resource (NSF ECCS-1542205), a node of NSF's NNCI network. TDTR measurements are supported by Office of Naval Research MURI grant N00014-16-1-2436 and are carried out in Frederick Seitz Materials Research Laboratory at the University of Illinois at Urbana-Champaign. F.E., E.F. and P.E. are funded by the Knut and Alice Wallenberg Foundation (2014.0226), the Swedish Research Council (2015-04153 and 2018-06482), and the FLAG-ERA JTC-2017 project MECHANIC funded by the Swedish Research Council (VR 2017-06819); they acknowledge the computer time allocations by the Swedish National Infrastructure for Computing at NSC (Linköping) and C3SE (Gothenburg). A.R. and electron microscopy at the Cornell Center for Materials Research are supported by the NSF MRSEC grant DMR-1719875. The Titan microscope was acquired with the NSF MRI grant DMR-1429155. F.M. acknowledges support by the NSF Graduate Research Fellowship Program under grant no. DGE-1746045. Y.Z. acknowledges support by the Camille and Henry Dreyfus Foundation, Inc., under the Dreyfus Environmental Postdoc award EP-16-094.

Author contributions S.E.K., J.S., and J.P. conceived the experiments. S.E.K. produced and performed the structural characterizations of the r-TMD films, and ran the finite-element simulations. F.M. and C.P. grew the TMD monolayers. A. Rai and D.G.C. performed the TDTR measurements. F.E., E.F. and P.E. conducted the atomistic simulations. P.P. fabricated the Au electrodes for the electromigration experiments. A. Ray and D.A.M. performed the STEM imaging. S.E.K. performed the Raman measurements and analysed the data with the help of D.G.C. and Y.Z. S.E.K., F.M. and J.P. wrote the manuscript. J.P., D.G.C. and P.E. oversaw the project. All authors discussed the manuscript and provided feedback.

Competing interests The authors declare no competing interests.

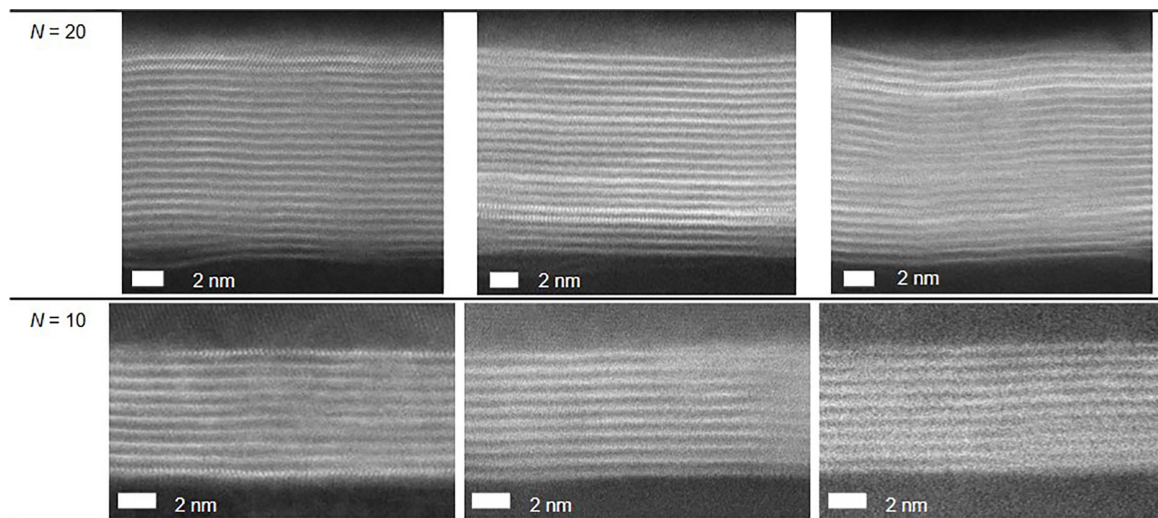
Additional information

Supplementary information The online version contains supplementary material available at <https://doi.org/10.1038/s41586-021-03867-8>.

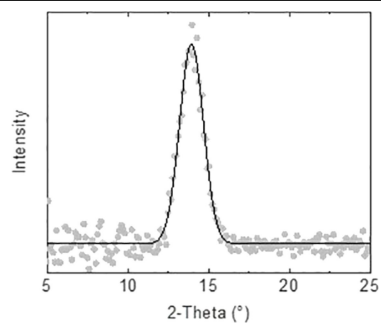
Correspondence and requests for materials should be addressed to Paul Erhart, David G. Cahill or Jiwoong Park.

Peer review information Nature thanks Davide Donadio, M. Muñoz Rojo and Mariusz Zdrojek for their contribution to the peer review of this work.

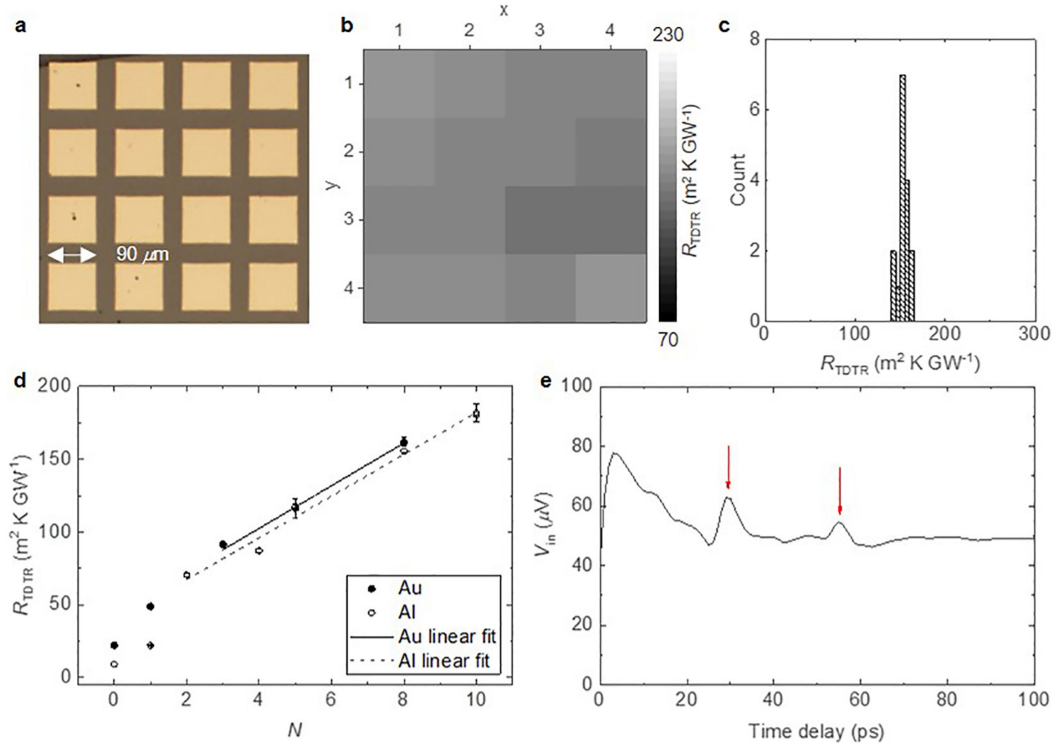
Reprints and permissions information is available at <http://www.nature.com/reprints>.



Extended Data Fig. 1 | Cross-sectional TEM images of $N = 20$ and $10 r\text{-MoS}_2$ on AlO_x . Each set of N images are taken from the same sample at different locations. The $N = 10$ films are coated with Al that was electron beam evaporated onto the surface.



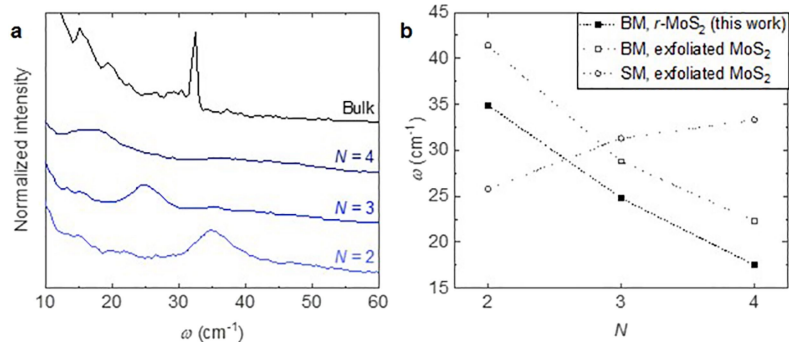
Extended Data Fig. 2 | GIWAXS data of $N = 10$ r-MoS₂. The peak position corresponds to a 2θ value of 14° , which translates to an interlayer spacing of 6.4 Å (scattering direction).



Extended Data Fig. 3 | Additional TDTR measurements and details.

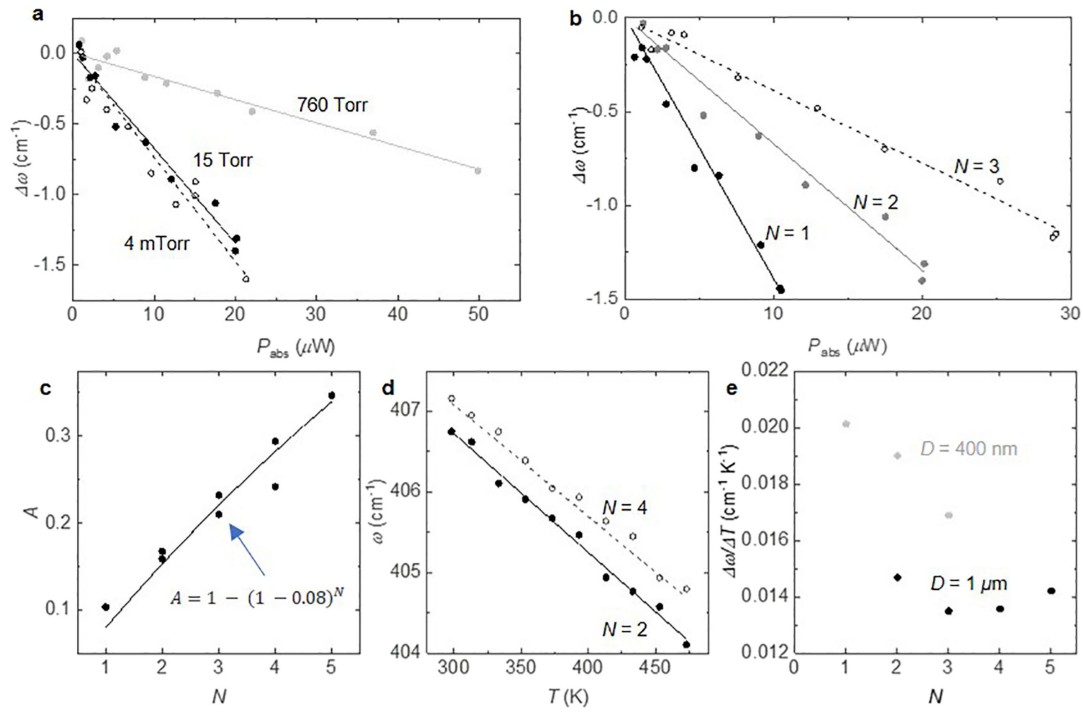
a, Microscope image of an $N=10$ r-MoS₂ film coated with a square grid of Al pads. **b**, 4×4 TDTR map of R_{TDTR} of an $N=10$ r-MoS₂ film. **c**, Histogram of R_{TDTR} array measurements. **d**, TDTR measurements of $N \leq 10$ r-TMD films coated with Au or Al. The error bars denote s.d.; number of TDTR measurements per film

sample, $n=3$ for Au samples; $n=3-5$ for the Al samples. **e**, Picosecond acoustics of a MoS₂ monolayer on thick sapphire substrate, coated with an Al transducer layer. The y-axis V_{in} is the in-phase signal of the lock-in amplifier. The red arrows indicate the acoustic waves reflected at the Al/MoS₂ interface.



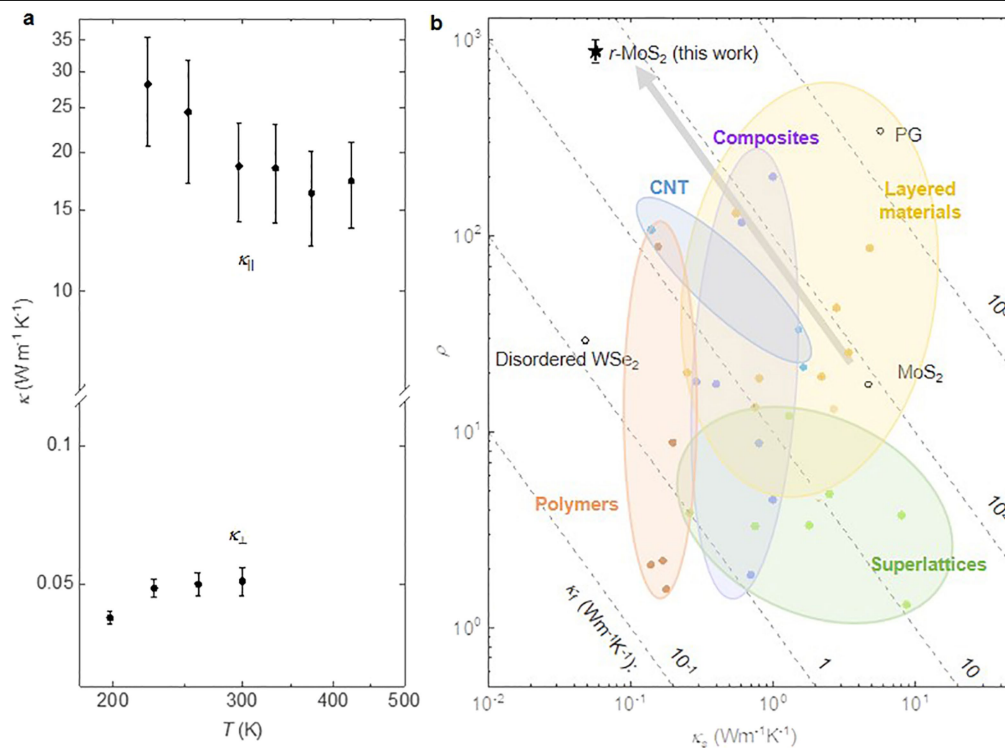
Extended Data Fig. 4 | Low-frequency Raman modes of r-MoS₂. **a**, Raman spectra reflecting the breathing modes (BM) of r-MoS₂ (blue) and the shear mode (SM) for MoS₂. **b**, The low-frequency Raman peak positions of r-MoS₂ and

exfoliated MoS₂. The filled squares indicate the BM peak positions of r-MoS₂. The open squares indicate the BM peak positions of exfoliated MoS₂, and the open circles indicate the SM peak positions of exfoliated MoS₂⁷².



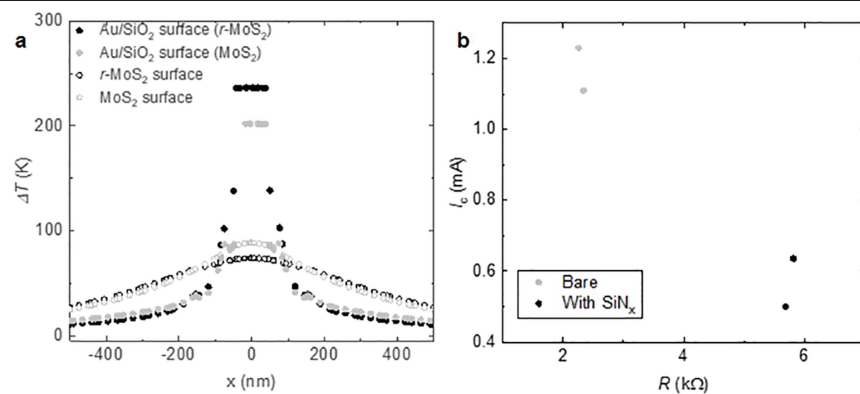
Extended Data Fig. 5 | Raman thermometry on r-MoS₂ films. **a**, $\Delta\omega$ - P_{abs} curves of representative $N=2$ r-MoS₂ films at different pressures. The P_{abs} values along the x axis are normalized to account for the slight differences in beam spot sizes ($\Delta r = 20\%$). The results at 15 torr and 4 mtorr signify no effect of reducing the pressure to below 15 torr. $\Delta\omega$ was approximately five-fold smaller at atmospheric pressure due to the extra heat loss channel by air. **b**, $\Delta\omega$ - P_{abs}

curves of r-MoS₂ films made up of $D=400$ nm (grain size) monolayers. **c**, Optical absorption of suspended r-MoS₂ films, which follows the trend $A = 1 - (1 - A_0)^N$, where A_0 is the monolayer absorptance. From the fit, $A_0 = 0.08 \pm 0.003$. **d**, ω - T calibration measurements of suspended r-MoS₂ films ($D=1$ μm), with the $N=2$ and $N=4$ data as the representative curves. **e**, ω - T slopes versus layer number for all films, with $D=400$ nm or 1 μm.



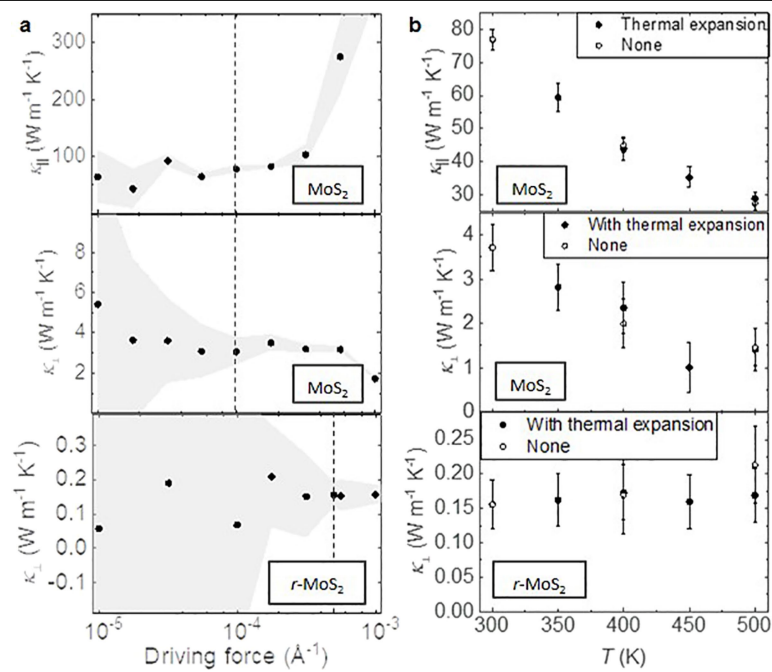
Extended Data Fig. 6 | $\kappa(T)$ and ρ of r-MoS₂. **a**, $\kappa(T)$ of r-MoS₂, with $\kappa_{||}$ measured using Raman thermometry of $N = 4$ r-MoS₂, and κ_{\perp} measured via TDTR as reported in Fig. 2c. The error bars are the propagated uncertainties from the calculation of the conductance value for each N . The error bars denote the propagated uncertainty of the calculations from the input parameters. We observed that $\kappa_{||}$ decreased with T , alluding to phonon-mediated heat transport

and attesting to the long-range crystallinity of the r-MoS₂ films in-plane. This was in contrast with the $\kappa_{\perp}(T)$ behaviour (Fig. 2c), which showed a slightly increasing trend. **b**, Catalogue of experimentally measured anisotropy ratios at room temperature versus slow-axis thermal conductivity (κ_s) of thermally anisotropic materials from literature, by category.



Extended Data Fig. 7 | r-MoS₂ efficacy as a heat spreader. a, Finite element simulations of the linear temperature profiles of Au electrodes covered with MoS₂ and r-MoS₂. **b**, SiN_x as heat spreaders for Au electrodes. Electrical properties of 10-nm-thick, 100-nm-wide and 10- μ m-long Au electrodes before

and after 16 nm SiN_x film deposition onto the electrodes using plasma-enhanced chemical vapour deposition. In contrast to r-MoS₂, the direct deposition of an ultrathin inorganic film such as SiN_x with a comparable κ to $\kappa_{||}$ of r-MoS₂ negatively affects the performance of the Au electrodes.



Extended Data Fig. 8 | Optimization of the MD simulations for κ calculations. **a**, Optimization of the driving force of the system, where the grey zone denotes the error. **b**, Effect of thermal expansion on κ .

Extended Data Table 1 | Comparison of literature thermal boundary resistances with experimentally measured values

General	
Time step	1 fs
Equilibration	
Run time	100 ps
Thermostat	Berendsen barostat (nvt.ber)
Thermostat coupling	0.01
Sampling	
Run time	1 ns
Thermostat	Nose-Hoover chains (nvt.nhc)
Thermostat coupling	500 fs
RTC interval	1000 steps
Driving force	1×10^{-4} eV / Å; 5×10^{-4} eV / Å for <i>r</i> -MoS ₂ in the z direction

Extended Data Table 2 | Parameters used in the calculations of the thermal conductivity using GPUMD

Interface	Thermal boundary resistance ($\text{m}^2 \text{ K GW}^{-1}$)	Reference
Al/MoS ₂ , R ₁	13-30	A. Sood et al., Nano Lett. , 2019
	20-29	P. Jiang et al., Adv. Mater. , 2017
MoS ₂ /sapphire, R ₂	27-53	X. F. Yue et al., J. Appl. Phys. , 2020
R ₁ + R ₂	40-83	
This work (experiment)	61 ± 7 (<i>r</i> -MoS ₂)	
	67 ± 3 (<i>r</i> -WS ₂)	